

A Pixon-Based Method for Reverberation-mapping Analysis in Active Galactic Nuclei

YAN-RONG LI ¹, MING XIAO,¹ AND JIAN-MIN WANG ^{1,2,3}

¹Key Laboratory for Particle Astrophysics, Institute of High Energy Physics, Chinese Academy of Sciences, 19B Yuquan Road, Beijing 100049, China; liyanrong@mail.ihep.ac.cn

²School of Astronomy and Space Science, University of Chinese Academy of Sciences, 19A Yuquan Road, Beijing 100049, China

³National Astronomical Observatories of China, Chinese Academy of Sciences, A20 Datun Road, Beijing 100012, China

ABSTRACT

We present an alternative method for reconstructing a velocity-delay map in reverberation mapping (RM) based on the pixon algorithm initially proposed for image reconstruction by Pina & Puetter. The pixon algorithm allows for a variable pixon basis to adjust resolution of each image pixel according the information content in that pixel, which therefore enables the algorithm to make the best possible use of measured data. The final optimal pixon basis functions would be those that minimize the number of pixons while still providing acceptable descriptions to data within the accuracy allowed by noises. We adapt the pixon algorithm to RM analysis and develop a generic framework to implement the algorithm. Simulation tests and comparisons with the widely used maximum entropy method demonstrate the feasibility and high performance of our pixon-based RM analysis. This paper serves as an introduction to the framework and the application to velocity-unresolved RM. An extension to velocity-resolved cases will be presented in a companion paper.

Keywords: galaxies: Active galaxies (17); Quasars (1319); Reverberation mapping (2019); Algorithms (1883)

1. INTRODUCTION

The reverberation mapping (RM) technique in active galactic nuclei (AGNs) measures responses of variations of reprocessing emissions to those of driving emissions (Blandford & McKee 1982; Peterson 1993). The responses as functions of time delay and wavelength (or velocity) generally decode information about geometry and kinematics of the reprocessing regions. Over the past three decades, the great successful application of RM to broad emission lines in AGNs had significantly advanced our understanding of the gaseous regions (the so-called broad-line regions, BLRs) responsible for broad emission lines (e.g., Kaspi et al. 2000; Bentz et al. 2013; Du et al. 2014, 2016) and, most importantly, yielded an efficient mass estimate of the central supermassive black holes (SMBHs, e.g., Peterson et al. 2004; Peterson 2014). Only with this mass estimate were systematic studies on cosmological evolution of SMBHs made possible (e.g., Marconi et al. 2004; Wang et al. 2009; Li et al. 2011, 2012; Kelly & Shen 2013; Shankar et al. 2013).

Another important application of RM is diagnosing structures of the accretion disk (e.g., Sergeev et al. 2005; Edelson et al. 2019; Cackett et al. 2020) and hot corona, a region believed to be located around the inner accretion disk and to mainly emit X-rays (e.g., Reynolds et al. 1999; Alston et al. 2020). The key finding toward this line, mainly revealed from the *Swift* intense accretion disk RM survey, was that UV/optical interband lags are consistent with the lag-wavelength relationship ($\tau \propto \lambda^{4/3}$) predicted by the standard accretion disk model. However, the amplitudes of interband lags are generally larger by a factor of ~ 2 than the

anticipated values (e.g., Edelson et al. 2019 and references therein). This had spurred extensive investigations over the accretion disk model itself and other physical processes possibly involved (e.g., Dexter & Agol 2011; Hall et al. 2018; Korista & Goad 2019; Sun et al. 2020).

In the coming era of massive time-domain surveys (e.g., the Zwicky Transient Facility, Bellm et al. 2019; the Large Synoptic Survey Telescope, Ivezić et al. 2008), the RM technique is expected to provide much more profound insight into geometry and kinematics of gaseous environments surrounding the vicinity of the central SMBHs. This calls for developing alternative sophisticated methods rather than using the traditional simple cross-correlation method to make the best use of information contained in measured data. Indeed, previously there had been several methods proposed/developed for this purpose, including the maximum entropy technique (Horne 1994), the regularized linear inverse method (Krolik & Done 1995), the SOLA method (Pijpers & Wanders 1994), and other forward methods with a presumption of AGN variability models (Zu et al. 2011; Li et al. 2016; Starkey et al. 2016). Among these methods, the maximum entropy technique had found several applications (e.g., Horne et al. 2003, 2020; Bentz et al. 2010; Grier et al. 2013; Xiao et al. 2018a,b) owing to its simple underlying principle and flexibility in describing the data and suppressing the noise propagation.

In the maximum entropy method (MEM), the entropy acts as a prior probability to a specific solution from a Bayesian viewpoint. In the absence of any additional information, this entropy prior states that the flattest solutions are the most probable. However, in reality, we expect that true mean-

ingful solutions deviate from flatness and show structures. In this sense, the default flatness is no longer an ideal prior, which instead should be assigned according to the information content in measured data and truly maximized with the best solutions¹. On the other hand, there are usually some parts in the solutions that are blank and have no information content. These blank parts should be assigned low weights or excluded from degrees of freedom. Considerations such as these led [Pina & Puetter \(1993\)](#) to introduce the pixion concept for image reconstruction. A variety of astronomical applications demonstrated high performance of the pixion method and its great capability in noise suppressing and robust rejection of spurious sources in image reconstructions ([Metcalf et al. 1996](#); [Puetter 1996](#); [Dixon et al. 1997](#); [Puetter & Yahil 1999](#); [Eke 2001](#)). Briefly speaking, a pixion is a generalized pixel and basic unit for image reconstruction. Pixions are able to vary in size to adapt to the measured data so as to make the information content flat across the inferred solutions in terms of pixions. Smallest pixions are used to describe regions with the highest information content, whereas large pixions are used for low signal-to-noise ratio (S/N) regions. The ultimate goal of the pixion method is to find the fewest pixions that still yield acceptable fits to the measured data. This is generally implemented in an iterative way, and the termination point is well defined.

The essence of RM analysis is deconvolving the integral equation

$$F_l(v, t) = \int \Psi(v, \tau) F_c(t - \tau) d\tau, \quad (1)$$

where $F_c(t)$ and $F_l(v, t)$ are observables that represent variations of the continuum and emission line at time t and velocity v , respectively, $\Psi(v, \tau)$ is the transfer function, and τ is the time lag. This is in analogy with an image reconstruction process, meaning that the pixion method can also be adapted to RM analysis. An unimportant difference is that in image reconstructions the transfer functions are known and the true images are to be determined; by contrast, in RM the situation is just the reverse, namely, the true images (or the continuum light curves) are known and the transfer functions are to be determined. However, this does not affect our application of the pixion concept to RM analysis at all.

In this paper, we adapt the pixion method and develop a mathematical framework to implement the pixion concept in RM analysis. We are only concentrated on the light curves of velocity-integrated emission-line fluxes (namely, velocity unresolved) so that the integral equation is simplified to

$$F_l(t) = \int \Psi(\tau) F_c(t - \tau) d\tau. \quad (2)$$

It is straightforward to extend the current framework to velocity-resolved RM analysis.

¹ It is worth mentioning that in the MEM one can design some sort of default prior images appropriately changing with the local image solutions, which partially surmounts the issue of the flat prior ([Skilling 1989](#); [Horne 1994](#)).

The paper is organized as follows. Section 2 describes the methodology of the pixion concept and application to RM analysis. Section 3 performs a number of simulation tests to verify the validity and feasibility of our pixion-based RM analysis. In Section 4, we make a comparison to the MEM. Discussion and conclusion are given in Section 5.

2. METHODOLOGY

In this section, we first briefly describe the pixion concept and the necessary formulae following the denotations in [Metcalf et al. \(1996\)](#). We then adapt the pixion method to RM analysis. Considering that observed light curves generally are irregularly sampled, we present two approaches for reconstructing continuum light curves on evenly spaced times. The first approach is based on the pixion concept, and the other is based on the damped random walk (DRW) process.

2.1. The Pixion Concept

According to Bayes' theorem, the posterior probability of the reconstructed image (I) and model (M) given the observed data (D) is written as

$$P(I, M|D) = \frac{P(D|I, M)P(I|M)P(M)}{P(D)} \propto P(D|I, M)P(I|M), \quad (3)$$

where $P(D|I, M)$ is likelihood probability, $P(D)$ is the marginal likelihood or evidence, $P(I|M)$ is the image prior that does not depend on the data, and $P(M)$ is the model prior that is generally presumed to be uniform.

By assuming that the measurement errors are independent and Gaussian, the likelihood probability reads

$$P(D|I, M) \propto \exp\left(-\frac{\chi^2}{2}\right), \quad (4)$$

where χ^2 is the sum of the squares of the standardized residuals (see below). The image prior can be quantified by considering the simple counting argument, namely, distributing N indistinguishable photons randomly among n_{pixion} pixions (or cells). By denoting the number of photons in pixion i to be N_i , the image prior of a particular distribution is

$$P(I|M) = \frac{N!}{n^N \prod_i N_i!} \propto \frac{1}{(n_{\text{pixion}})^N} \exp(S), \quad (5)$$

where Stirling's approximation to factorials is used to derive the far right-hand side and

$$S = - \sum_{i=1}^{n_{\text{pixion}}} \frac{N_i}{N} \ln \frac{N_i}{N}. \quad (6)$$

Here we note that the summation runs over pixions instead of pixels.

As can be seen, the image prior probability increases as the number of pixions decreases. This is why the pixion method seeks to find the fewest number of pixions. The exponential term in Equation (5) can be deemed to be a sort of entropy

as in the MEM. With Equations (4) and (5), the posterior probability is given by

$$P(I, M|D) \propto \frac{1}{(n_{\text{pixon}})^N} \exp \left[-\frac{1}{2} (\chi^2 - 2S) \right]. \quad (7)$$

In practice, the ratio N_i/N can be recast into I_i/I_{tot} , where I_i is the physical quantity (to be solved) in the i -th pixion and $I_{\text{tot}} = \sum_i I_i$. However, there is not a clear way to calculate the total photon number N considering that we are concentrated on solving the transfer functions. It is thus not straightforward to directly explore this posterior probability defined above. We note that the factor $1/(n_{\text{pixon}})^N$ is maximized provided that the pixion number is as small as possible. As a result, optimizing the above posterior probability is indeed bound to maximize the exponential term in Equation (7), as well as find the fewest number of pixions.

To implement the pixion concept, Pina & Puetter (1993) introduced the fractal pixion basis, which is a family of chosen functions with various widths. The reconstructed image $I(x)$ is then represented as a convolution of a pseudo-image $I^{(p)}(x)$ with a pixion basis function appropriate at pixel x ,

$$I(x) = \int I^{(p)}(y) K_x \left(\frac{y-x}{\delta_x} \right) dV_y, \quad (8)$$

where δ_x is the width of the pixion basis function K_x , which is normalized such that

$$\int K_x \left(\frac{y}{\delta_x} \right) dV_y = 1. \quad (9)$$

In this implementation, each pixion shares some fraction of signals from its adjacent pixions and there are no hard edges between pixions. The pixion density at i -pixel is

$$f_i = \left[\int k_i \left(\frac{y}{\delta_i} \right) dV_y \right]^{-1}, \quad (10)$$

where k_i is the pixion basis function normalized to 1 at $y = 0$. The number of pixions is the sum of f_i over all pixels, namely (Metcalf et al. 1996),

$$n_{\text{pixon}} = \sum_{i=1}^{n_{\text{pixel}}} f_i, \quad (11)$$

where n_{pixel} is the number of pixels. The entropy term in Equation (7) can be recast into the summation over pixels as (Metcalf et al. 1996)

$$S = - \sum_{i=1}^{n_{\text{pixel}}} \frac{N_i}{N} \ln \frac{N_i}{f_i N} \approx -\alpha \sum_{i=1}^{n_{\text{pixel}}} \frac{N_i}{N} \ln \frac{N_i}{N}, \quad (12)$$

where on the right-hand side N_i refers to i -pixel and again N_i/N can be replaced with I_i/I_{tot} to make it calculable, and

$$\alpha = \frac{\ln n_{\text{pixon}}}{\ln n_{\text{pixel}}}. \quad (13)$$

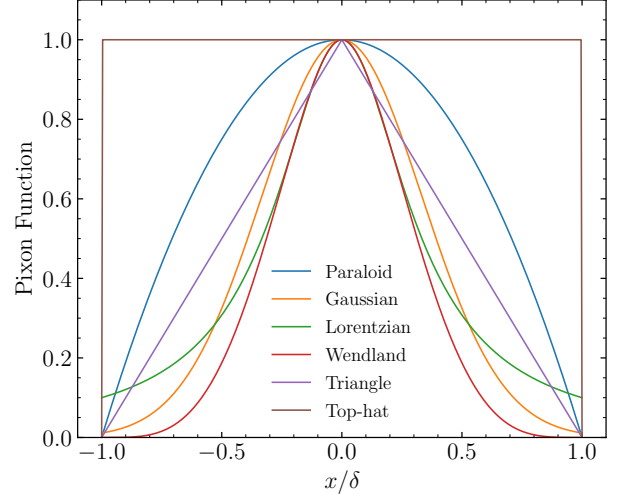


Figure 1. Shapes of pixion basis functions listed in Table 1. The pixion functions are truncated at $x = \pm\delta$.

Table 1. Pixion shapes and normalizations.

Name	Shape	Normalization
Paraboloid	$1 - \frac{x^2}{\delta^2}$	$\frac{3}{4\delta}$
Gaussian	$\exp\left(-\frac{1}{2} \frac{9x^2}{\delta^2}\right)$	$\left[\sqrt{2\pi} \operatorname{erf}\left(\frac{3}{\sqrt{2}}\right) \frac{\delta}{3} \right]^{-1}$
Lorentzian	$\frac{1}{1+9x^2/\delta^2}$	$\left[\frac{2\delta}{3} \tan^{-1}(3) \right]^{-1}$
Wendland	$\left(1 - \frac{ x }{\delta}\right)^4 \left(4 \frac{ x }{\delta} + 1\right)$	$\frac{3}{2\delta}$
Triangle	$1 - \frac{ x }{\delta}$	$\frac{1}{\delta}$
Top hat	1	$\frac{1}{2\delta}$

NOTE—All pixion functions are truncated at $|x| = \delta$, beyond which the function values vanish.

The entropy term is indeed not important in the pixion method because pixions already induce effective smoothing to make solutions as flat as possible (Metcalf et al. 1996).

There are no restrictions on selection of the pixion basis functions *a priori*. Truncated paraboloids were widely adopted in applications of the pixion concept (Pina & Puetter 1993; Metcalf et al. 1996; Dixon et al. 1997) largely because of the computational demands. The other functions, such as truncated Gaussians, were also adopted (Eke 2001). We list several pixion basis functions and their normalizations in Table 1 and plot the corresponding shapes in Figure 1. In most cases, the results are not sensitive to the selection of pixion basis functions. However, these pixion basis functions with sharp edges (e.g., top hats) would be more likely to produce unsmoothed features in reconstructed images, which are not always desirable.

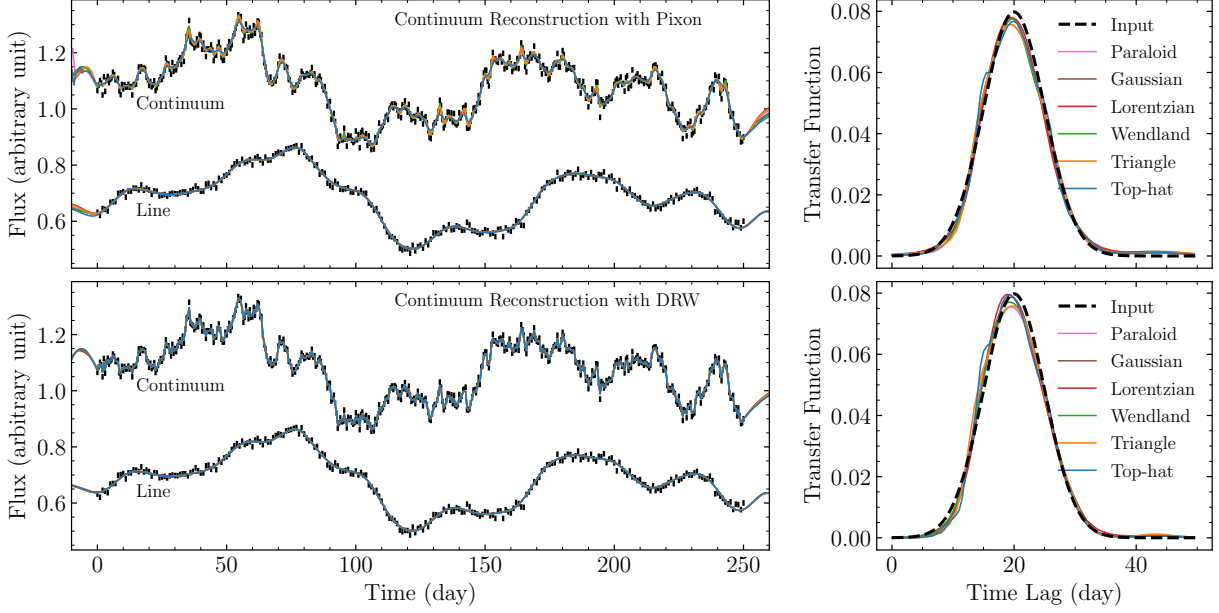


Figure 2. Validity tests of our pixion-based approach for RM analysis. Top panels show results for the case of continuum reconstruction using the pixion concept, and bottom panels are for the case of continuum reconstruction using DRW. In each case, the left panel shows the simulated light curves of continuum and emission line (black error bars) and their reconstruction (solid lines), and the right panel shows reconstructed transfer functions with different pixion basis functions listed in Table 1. Black solid lines represent the input transfer function.

2.2. Application to Reverberation Mapping

In RM analysis, the quantity to be determined is the transfer function $\Psi(\tau)$ in Equation (2). Following the nomenclature introduced in the preceding section, we use the term “image” to represent the transfer function and I_i to denote its value at i -pixel. The chi square for the emission-line data D_l is

$$\chi_l^2 = \sum_j \frac{(F_{l,j} - D_{l,j})^2}{\sigma_{l,j}^2}, \quad (14)$$

where $D_{l,j}$ and σ_j are the measured flux and error of the emission line at time t_j , respectively, and $F_{l,j}$ is the reconstructed flux using Equation (2).

To implement the convolution of Equation (2), one needs to reconstruct continuum fluxes from the usually irregularly sampled continuum light curve. We present two approaches for this purpose: one is based on the pixion method itself, and the other is based on the DRW process.

2.2.1. Continuum Reconstruction Using the Pixion Concept

Similar to the above-mentioned pixion concept, we can also use pixions to reconstruct continuum light curve as

$$F_c(t) = \int F_c^{(p)}(t') K_t \left(\frac{t-t'}{\delta_t} \right) dt', \quad (15)$$

where $F_c^{(p)}$ is the pseudo-continuum to be determined, K_t is the pixion function appropriate at time t and δ_t is the width of the pixion function. The chi square of continuum reconstruction is

$$\chi_c^2 = \sum_j \frac{(F_{c,j} - D_{c,j})^2}{\sigma_{c,j}^2}, \quad (16)$$

where $D_{c,j}$ and $\sigma_{c,j}$ are the measured flux and error of the continuum at time t_j . For simplicity, we use a uniform pixion size for continuum reconstruction.

2.2.2. Continuum Reconstruction Using the DRW Process

With the DRW process, the continuum reconstruction is given by (Rybicki & Press 1992; Li et al. 2018)

$$F_c(t) = (\mathbf{Q}^{1/2} \boldsymbol{\xi}_s + \hat{\delta}) + \mathbf{L}(\mathbf{C}_q^{1/2} \boldsymbol{\xi}_q + \hat{\mathbf{q}}), \quad (17)$$

where \mathbf{L} is a vector with all unity elements, $\boldsymbol{\xi}_s$ and $\boldsymbol{\xi}_q$ are random variables following a normal distribution, and

$$\begin{aligned} \mathbf{C}_q &= (\mathbf{L}^T \mathbf{C}^{-1} \mathbf{L})^{-1}, \\ \mathbf{Q} &= [\mathbf{S}^{-1} + \mathbf{N}^{-1}]^{-1}, \\ \hat{\mathbf{q}} &= \mathbf{C}_q \mathbf{L}^T \mathbf{C}^{-1} \mathbf{y}_c, \\ \hat{\delta} &= \mathbf{S} \mathbf{C}^{-1} [\mathbf{y}_c - \mathbf{L}(\mathbf{C}_q^{1/2} \boldsymbol{\xi}_q + \hat{\mathbf{q}})]. \end{aligned} \quad (18)$$

Here \mathbf{y}_c represents the measured continuum light curve, $\hat{\mathbf{q}}$ represents the best estimate for the mean of the continuum light curve, $\hat{\delta}$ represents the best estimate for the underlying variation signal, \mathbf{N} is the covariance matrix of the measurement errors, \mathbf{S} is the covariance matrix of the variation signal, and $\mathbf{C} = \mathbf{S} + \mathbf{N}$. For a DRW process, the covariance depends on time difference Δt as

$$S(\Delta t) = \sigma_d^2 \exp\left(-\frac{|\Delta t|}{\tau_d}\right), \quad (19)$$

where σ_d and τ_d are two parameters, which represent the standard deviation of variations on a long-term timescale and the typical timescale of variations, respectively.

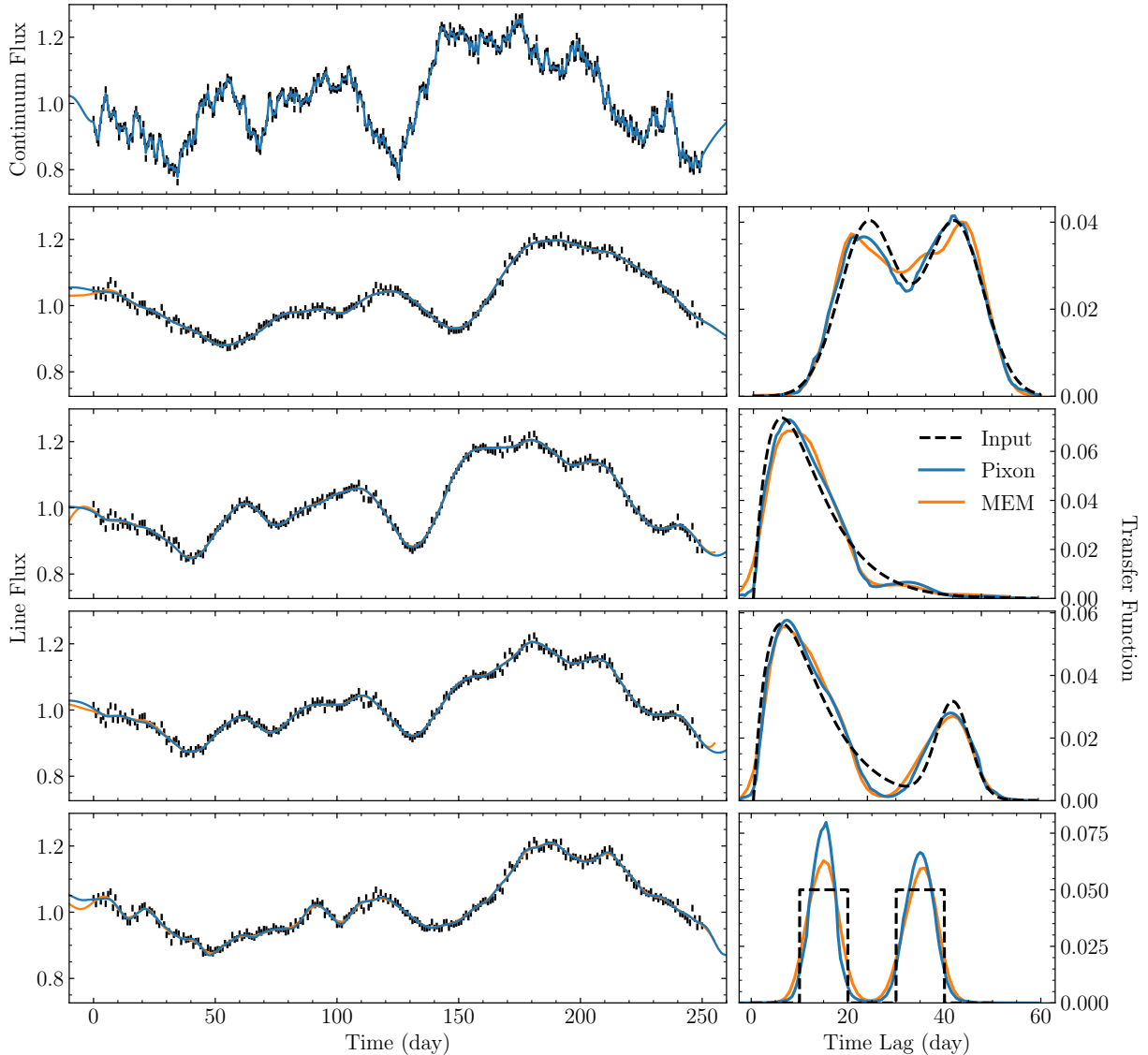


Figure 3. Validity tests of our pixion-based approach with various shapes of input transfer functions: two highly blending Gaussians, a fast-rising peak with a long-descending tail, a fast-rising peak with a long-descending tail plus a Gaussian, and two displaced top hats (top to bottom). The top left panel shows the generated continuum light curve. Four panels underneath show simulated light curves of the emission line using the transfer functions plotted in the right panels (black dashed lines). Blue solid lines represent reconstructions to the light curves and recovered transfer functions. The pixion basis functions are set to Gaussian. In the top left panel, only the reconstruction to the continuum light curve for the case of two highly blending Gaussians is plotted. For the sake of comparison, the reconstructions to light curves and transfer functions by the MEM are also superposed (yellow solid lines).

The parameter set for continuum reconstruction with the DRW process includes σ_d , τ_d , ξ_s , and ξ_q . Once σ_d and τ_d are given, the matrices \mathcal{S} , \mathcal{C} , \mathcal{C}_q , and \mathcal{Q} in Equations (17) and (18) will be uniquely determined. To simplify calculations, we determine the best values of σ_d and τ_d by only optimizing the posterior probability for the continuum light curve (see Li et al. 2018). In subsequent RM analysis, we then fix σ_d and τ_d with the best values but set ξ_s and ξ_q as free parameters. As such, there is no need to calculate the above matrices and their determinants every step of RM analysis, and therefore the computational speed will be significantly improved.

Note that in this procedure the continuum reconstruction is already best optimized, and therefore the chi square for continuum reconstruction is no longer necessary.

2.3. Optimization

As described above, in the pixion concept, to optimize the posterior probability of Equation (7), we alternatively maximize the exponential term of the posterior probability and meanwhile find the fewest allowed number of pixions. As a result, there are two aspects for optimization: determining the best pixion map that specifies the pixion size at each pixel

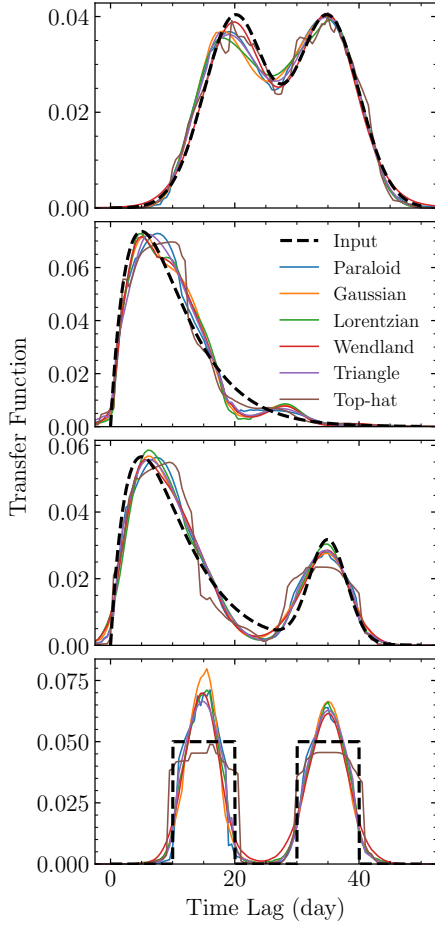


Figure 4. Tests on various shapes of transfer functions with different pixion basis functions. From top to bottom panels, the shapes of input transfer functions are two highly blending Gaussians, a fast-rising peak with a long-descending tail, a fast-rising peak with a long-descending tail plus a Gaussian, and two displaced top hats. The simulated continuum and line light curves are the same as in Figure 3. The continuum light curves are reconstructed using DRW.

and the best solutions for the transfer function. This is generally implemented in an iterative manner. First, we presume a pixion map, and with this pixion map fixed, we solve for the best solution of the transfer function. Then with the solution of the transfer function fixed, we update the pixion map. We iterate this recipe until the termination conditions are satisfied.

We rewrite the exponential term of the posterior probability (Equation 7) in logarithm

$$\ln P(I, M|D) \propto -(\chi^2 + 2S). \quad (20)$$

The expressions for χ^2 and S are slightly different between the two approaches of continuum reconstructions described in Section 2.2. (1) For continuum reconstruction with the pixion concept, the total chi square is the sum of

$$\chi^2 = \chi_l^2 + \chi_c^2. \quad (21)$$

Similarly, the total entropy is the sum of

$$S = S_l + S_c, \quad (22)$$

where S_l and S_c are the entropies for line and continuum reconstruction, respectively. (2) For continuum reconstruction with the DRW process, there is no need to include the chi square and entropy term for continuum reconstruction, so that $\chi^2 = \chi_l^2$ and $S = S_l$. We use a truncated Newton algorithm developed by Nash (1984) to maximize Equation (20). This needs to calculate gradients of χ^2 and S with respect to parameters. In the Appendix, we present derivations for these gradients.

Following Metcalf et al. (1996), we start with a pixion map that has the largest, uniform pixion size. This ensures that we compute the large-scale structures in the image before resolving the small-scale structures. We then iterate the image and pixion map with the above two-step recipe and gradually reduce the pixion sizes. To examine whether the pixion size at i -pixel is allowed to reduce, we calculate the differential

$$\Delta G = \Delta \delta_i \frac{\partial G}{\partial \delta_i}, \quad (23)$$

where $G = \chi^2 + 2S$. In the meantime, the number of degrees of freedom at i -pixel also is subject to a change

$$\Delta f_i = \Delta \delta_i \frac{\partial f_i}{\partial \delta_i}, \quad (24)$$

where f_i is defined by Equation (10). We note that ΔG can also be deemed to be a change in the number of degrees of freedom. In this sense, the condition for reducing the pixion size is (Metcalf et al. 1996)

$$-\Delta G > \Delta f_i + \sigma \frac{\Delta f_i}{\sqrt{2f_i}}, \quad (25)$$

where σ is a factor to control the sensitivity of reducing pixion sizes, $\sqrt{2f_i}$ is the expected standard deviation of the χ^2 -distribution with a degree of freedom of f_i , and the minus sign to ΔG comes from the fact that G decreases while f_i increases with decreasing δ_i . If the condition at a pixel is satisfied, the pixion size at that pixel is reduced; if not, the previous pixion size is retained. The pixion map is updated once all pixels are tested, and the overall iteration is terminated if there is no further update to the pixion map.

3. TESTS

We perform basic tests on our pixion-based approach for RM analysis by simulating a number of artificial light curves with given power spectral density (PSD) models (e.g., Li & Wang 2018). Unless stated otherwise, the simulations are set up as follows. We use the DRW process (see Equation 19) to generate light curves, which has a PSD form of²

$$P(\nu) = \frac{2\sigma_d^2 \tau_d}{1 + (2\pi \tau_d \nu)^2}. \quad (26)$$

² We note that in the literature PSDs may differ by constant factors, depending on adopted normalizations (Deeming 1975).

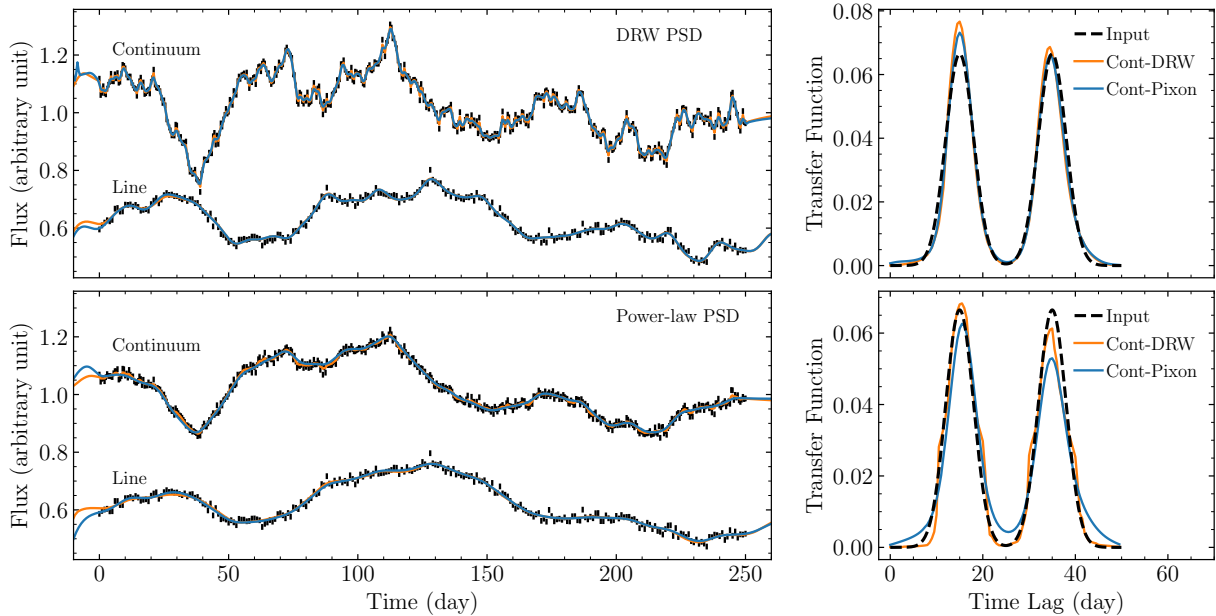


Figure 5. Tests with different variation models. Left: simulated light curves using the DRW process in the top panel and the power-law PSD in the bottom panel. Right: reconstructions to the input transfer function composed of two displaced Gaussians. Blue and yellow lines represent the approaches of continuum reconstruction using the pixion concept and DRW process, respectively (see Sections 2.2.1 and 2.2.2). We use the same random seed so that the global patterns of the simulated light curves are similar. The pixion basis functions are set to Gaussian.

We fix the parameters $\sigma_d = 0.15$ (arbitrary unit) and $\tau_d = 50$ days. The total time lengths are set to 250 days and the means of generated light curves are about one (arbitrary unit; subject to random fluctuations). The S/N ratios are about 100. The values of the model parameters adopted above typically result in variation amplitudes of 30%-50%.

3.1. Validity Tests

We first test the validity of our pixion-based approach. We randomly generate a continuum light curve with the DRW process. The cadence is 0.5 days apart. The light curve of emission line is obtained by convolving the continuum light curve with a Gaussian transfer function. The Gaussian has a center of 20 days and standard deviation of 5 days. The cadence of the emission-line light curve is 1 day apart. The left panels of Figure 2 plot the generated light curves of the continuum and emission line. We then use the different pixion basis functions listed in Table 1 to recover the transfer function. In Figure 2, the top right panel shows results for the case of continuum reconstruction using the pixion concept (see Section 2.2.1), and the bottom panel is for the case of continuum reconstruction using DRW (see Section 2.2.2). The right two panels of Figure 2 plot the correspondingly recovered transfer functions. We can find that all pixion basis functions yield Gaussian-like transfer functions well consistent with the input.

In Figure 3, we show the recovery to various shapes of input transfer functions, including two highly blending Gaussians, a fast-rising peak with a long-descending tail, a fast-rising peak with a long-descending tail plus a Gaussian, and two displaced top hats. We only use the DRW process to re-

construct the continuum and the Gaussian pixion basis functions. As can be seen, the major structures in the input transfer functions are overall well produced, although some sharp or discontinuous features are not captured because the pixion concept still favors smoothing solutions. Nevertheless, the above tests illustrate that the application of the pixion concept to RM analysis is feasible.

We note that the generated light curves in this section are somehow ideal in terms of data cadences. Below we will explore the performance of our approach under different simulation configurations.

3.2. Different Pixion Bases

Figure 2 illustrates the overall consistent recovery to a simple Gaussian transfer function with different pixion basis functions. In this section, we test the performance of pixion basic functions on more complicated transfer functions. In Figure 4, we implement our pixion-based approach on the same simulated light curves generated in Figure 3 with the pixion basic functions listed in Table 1. The continuum light curves are reconstructed using DRW. The input transfer functions have the same shapes as in Figure 3, namely, two highly blending Gaussians, a fast-rising peak with a long-descending tail, a fast-rising peak with a long-descending tail plus a Gaussian, and two displaced top hats. We can find that all pixion basic functions overall reproduce the major features in the input transfer functions. As mentioned above, the top-hat pixion basic function with hard edges is more inclined to yield unsmoothed small-scale features in transfer functions. We inspect the reconstructed light curves and do not find any significant differences with those reconstructed by

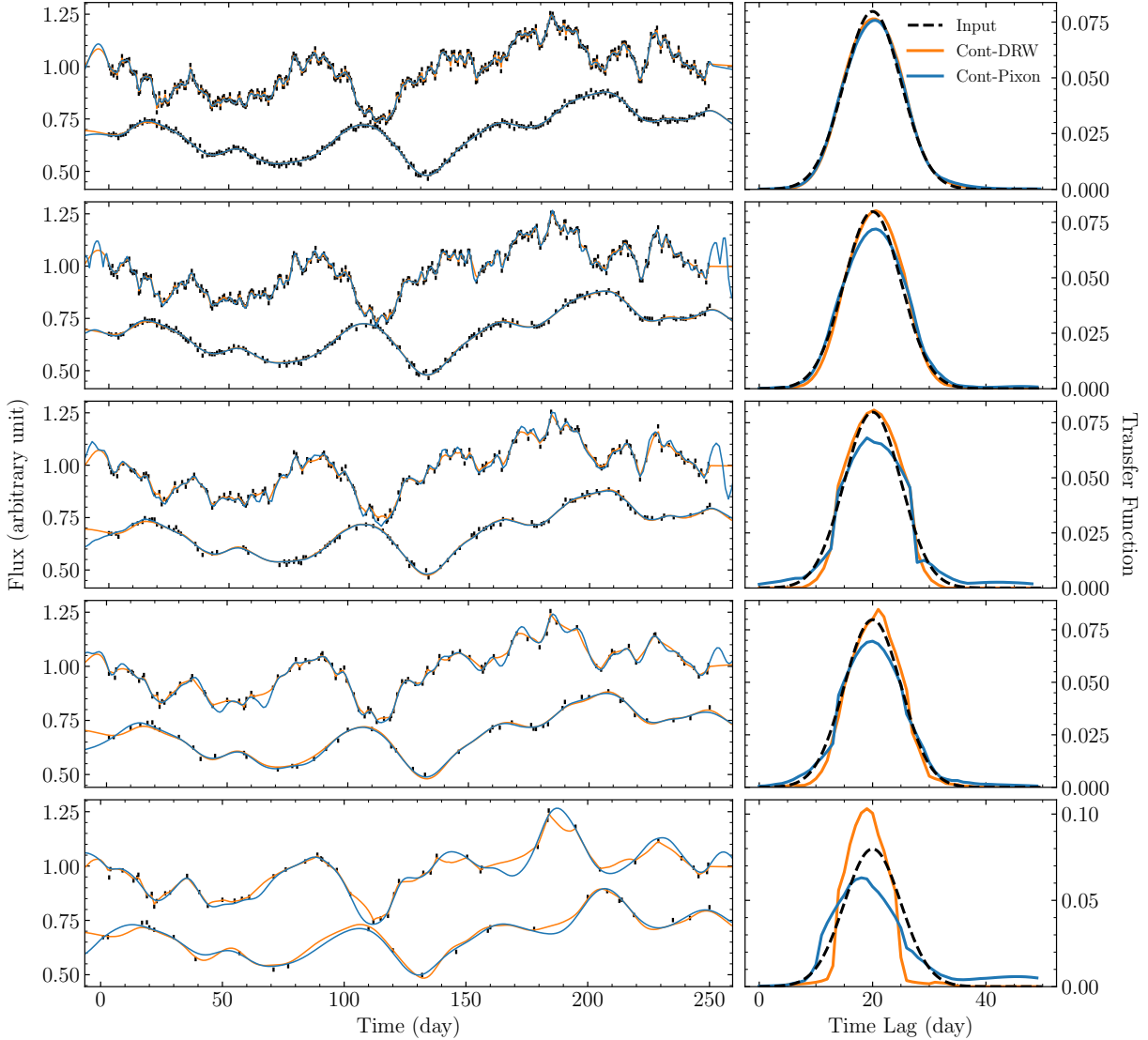


Figure 6. Tests with different cadences. Blue and yellow lines represent the approaches of continuum reconstruction using the pixion concept and DRW process, respectively (see Sections 2.2.1 and 2.2.2). The pixion basis functions are set to Gaussian.

other pixion basic functions. Nevertheless, the bottom panel of Figure 4 demonstrates that the top-hat basic function may be superior in capturing very sharp features in transfer functions.

3.3. Different Variation Models

To verify whether our approach depends on variation models of light curves, besides the DRW model, we also use a power-law PSD with a form of

$$P(\nu) = A \left(\frac{\nu}{10^{-2} \text{ day}^{-1}} \right)^{-\alpha}. \quad (27)$$

We set $A = 0.3$ (arbitrary unit) and $\alpha = 3$. The power-law PSD is forced to flatten to a constant below $5 \times 10^{-3} \text{ day}^{-1}$ to alleviate the issue of spectral power leakages (Uttley et al. 2002). The left panels of Figure 5 plot randomly generated light curves using the DRW process and power-law

PSD. We use the the same random seed in the two PSD models so that the global patterns of the light curves are similar. As expected, the light curve generated by the DRW process has much more significant short-timescale variations. The right panels of Figure 5 show reconstructions to the input transfer function composed of two displaced Gaussians using the two approaches for continuum reconstructions (see Sections 2.2.1 and 2.2.2). The approach based on the DRW process presumes that the continuum variations follow a DRW process, whereas the approach based on the pixion concept is less model dependent. Figure 5 demonstrates that the two peaks in the input transfer function are overall well reproduced in both approaches.

3.4. Different Data Cadences and Errors

In Figure 6, we first generate a continuum light curve and then gradually censor some fraction of data points randomly

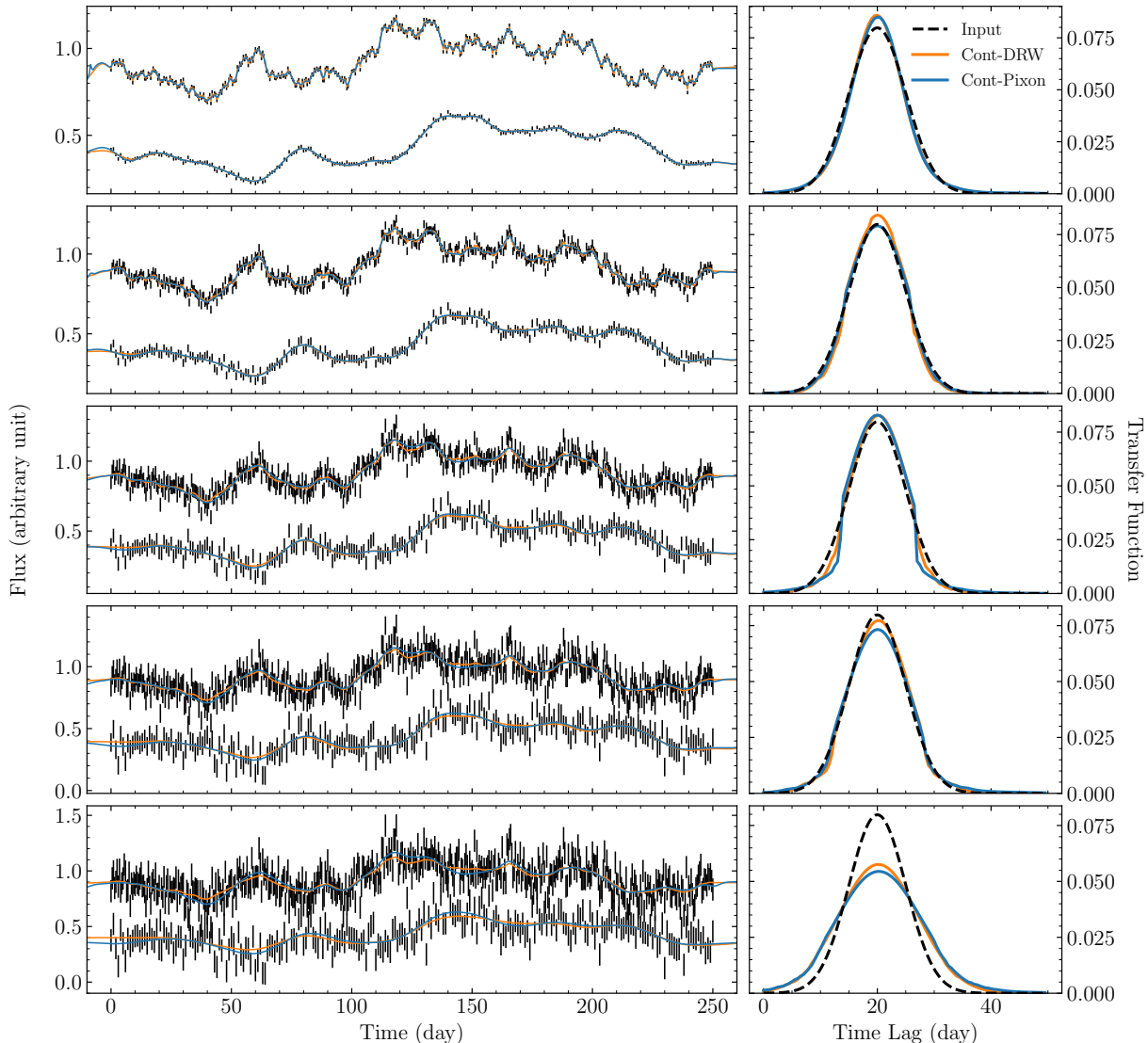


Figure 7. Tests with different errors. Blue and yellow lines represent the approaches of continuum reconstruction using the pixion concept and DRW process, respectively (see Sections 2.2.1 and 2.2.2). The pixion basis functions are set to Gaussian.

to simulate the influence of different cadences. From top to bottom panels of Figure 6, the mean cadences of the continuum light curves are set to 0.5, 0.7, 1.3, 2.3, and 5 days apart and the mean cadences of the emission-line light curves are set to 1, 1.3, 2.3, 5, and 10 days apart. In the first four cases, the recovered transfer functions are generally consistent with the input Gaussian transfer function. In the last case, where the sampling interval (10 days) of the emission-line light curve increases to one-half of the mean time lag of the input transfer function (20 days), the obtained transfer function displays mild deviations in the peak location, in particular for the continuum reconstruction using the pixion concept (see Section 2.2.1). We ascribe these deviations to the reason that the information contained in the light curves does not suffice to constrain the underlying variations appropriately. Notwithstanding, the peak-like shapes in the transfer function are still retained.

In Figure 7, we do testing with different errors. The typical S/Ns of the five pairs of generated light curves are set to 100, 40, 20, 13, and 10 from the top to bottom panels of Figure 7. Again, only the Gaussian pixion basis functions are used. The obtained transfer functions are in good agreement with the input in both shape and amplitude for the four cases with $S/N > 13$. For the case of $S/N = 10$, the obtained transfer functions have the same centers of time lags as the input but with slightly broader widths.

4. COMPARISON WITH THE MAXIMUM ENTROPY METHOD

The pixion method can be regarded as an extension of the MEM in the sense that it allows us to adjust the image prior according to the information content of the data. In the MEM, one can also design some forms of default prior images to steer the solutions toward those forms of priors as

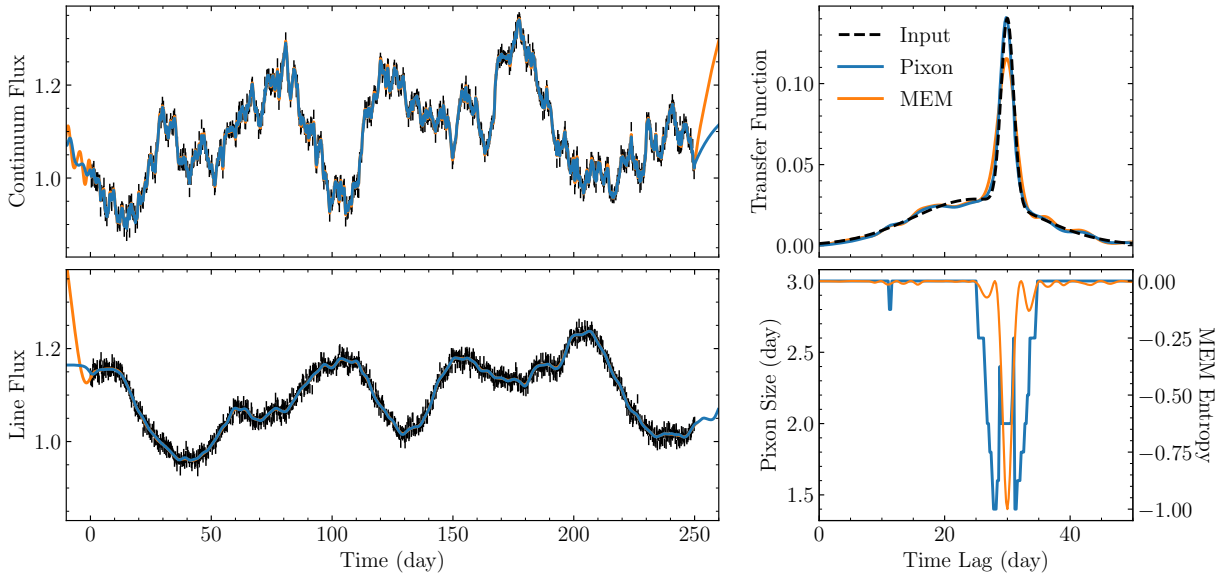


Figure 8. A comparison with the MEM on intensively sampled artificial light curves. Left: artificial light curves of the continuum and emission line. Blue and yellow solid lines represent reconstructions with our pixion method and the MEM, respectively. Top right: reconstructed transfer functions using our pixion method (blue) and the MEM (yellow). Bottom right: obtained pixion size distribution with time lag by our pixion method and entropy distribution by the MEM. The MEM entropy is normalized by the absolute of the minimum value.

closely as possible under the constraints of the data. For example, Horne (1994) chose the “curvature default” prior, approximately equivalent to minimizing curvatures of the solutions (in logarithm). By contrast, the pixion method does not assign default prior images explicitly; instead, it seeks to smooth the solutions locally as much as the data permit with the fewest number of pixions (namely, minimum complexity). It seems that this provides a natural and generic way to implement the principle of *Ockham’s Razor* (Puetter & Yahil 1999), a common rule of thumb in model selections via marginal likelihood maximization. As such, the issue of overresolution or underresolution are minimal in pixion solutions. Meanwhile, because the pixion method finds the fewest number of pixions, the termination condition in the iterative implementation can be well specified (see Section 2.3), which involves not only the goodness of fit (i.e., χ^2), but also the number of pixions. In comparison, the MEM mainly relies on adjusting a weight parameter (α), which controls the trade-off between the goodness of fit and entropy, to enforce the reduced χ^2 to approximate unity. This is one of the major differences between the pixion method and the MEM.

In Figure 3, we superpose the transfer functions obtained by the MEM for the sake of comparison. Here, we use the MEM implementation of Xiao et al. (2018a), which adopts the “curvature defaults” following Horne (1994). The results obtained by the both approaches are generally consistent with the input transfer functions. A noticeable difference revealed in the bottom right panel of Figure 3 and the bottom panel of Figure 4 is that the pixion method is relatively more capable of producing sharp features.

We further design a test with an extreme transfer function composed of a broad Gaussian and very narrow Gaus-

sian. The light curves are generated with a high cadence (0.2 days apart) to provide adequate information to recover the narrow Gaussian component. We run the pixion method and the MEM on the light curves and show the results in Figure 8. The broad Gaussian component in the transfer function is well reproduced by both the pixion method and the MEM, although there appear to be some very minor ripple-like features. However, for the narrow Gaussian component, the MEM seems to yield a slightly larger width, whereas the pixion method obtains a remarkably consistent width. In the bottom right panel of Figure 8, we show the pixion size distribution with time lag obtained by the pixion method and the entropy distribution obtained by the MEM. As Horne (1994) pointed out, the entropy with “curvature defaults” results in preference to solutions with Gaussian peaks ($\propto \exp(-\tau^2/2)$) and exponential tails ($\propto \exp(-\tau)$). The former have constant curvatures, and the latter have zero curvatures, both of which maximize the entropy. This might be the reason responsible for the resulting slightly larger width of the narrow Gaussian component. For the pixion results, we can find that the pixion size reaches a minimum around time lags where the transfer function changes the most rapidly, instead of around the peak of the transfer function. This is consistent with the expectation that high resolutions are required to recover rapid changing features in the transfer function.

5. DISCUSSION AND CONCLUSION

We adapt the pixion algorithm initially proposed for image reconstruction by Pina & Puetter (1993) to RM analysis and develop a generic framework to implement the algorithm. The pixion method uses pixions (instead of pixels) as the basic unit, which are able to adjust pixion sizes to achieve locally optimal resolutions according to the information con-

tent provided by the data. Within a pixion, the pixion algorithm smooths the solutions as much as the data allow. The terminated criterion of the pixion method is to find the fewest number of pixions that still adequately fit the data. This naturally obeys the principle of *Ockham's Razor* (Puetter & Yahil 1999). As such, the pixion method optimizes solutions not only by testing the goodness of fit but also by reducing the complexity to be optimal. The issue of overresolution or underresolution of the solutions is also significantly alleviated. In this sense, the pixion method is flexible to optimize the complexity of the solutions and can be regarded as a subcase of marginal likelihood maximization.

We perform a number of simulations to illustrate the validity of our pixion-based approach for RM analysis. We also compare the pixion method with the widely used MEM on simulated light curves (see Figures 3 and 8) and find that both the approaches generally give consistent results to the input transfer functions. However, in some cases, the pixion method performs better in producing sharp features in transfer functions.

There are several potential improvements to be made to our pixion-based RM analysis in future: (1) Currently, we only apply the pixion algorithm to velocity-unresolved RM analysis. It is straightforward to extend the current framework to velocity-resolved cases. Accordingly, the pixion basis should be functions of time lag and velocity. This might need some elaboration on the extensions of pixion basis functions along time lag and velocity directions. (2) We adopt the truncated Newton algorithm developed by Nash (1984) to seek the opti-

mized solutions. This algorithm does not require us to supply the Hessian information. In our pixion method, it is easy to analytically calculate the Hessian matrix; therefore, other optimization algorithms that make use of the Hessian information are worthwhile to apply to expedite the computational efficiency. (3) Our present pixion method is unable to estimate the uncertainties of the obtained solutions. A Markov Chain Monte Carlo may help to achieve this purpose.

We finally mention that the present approach applies not only to RM analysis of emission lines but also to RM analysis on multiband continuum light curves. We developed a software package `PIXON` for our pixion method and made it publicly available at <https://github.com/LiyuAstroph/PIXON>.

ACKNOWLEDGMENTS

This research is supported in part by the National Key R&D Program of China (2016YFA0400701); by grant Nos. NSFC-11833008, -11991051, and -11991054 from the National Natural Science Foundation of China; and by the China Manned Space Project with No. CMS-CSST-2021-A06 and CMS-CSST-2021-B11. Y.-R.L. acknowledges financial support from the National Natural Science Foundation of China through grant No. 11922304, from the Strategic Priority Research Program of CAS through grant No. XDB23000000, and from the Youth Innovation Promotion Association CAS. X.M. acknowledges financial support from the National Natural Science Foundation of China through grant No. 12003036.

APPENDIX

In this appendix, we present calculations of the gradients required to supply to the truncated Newton algorithm. The parameter set to be solved includes $I^{(p)}$, $F_c^{(p)}$, ξ_s , and ξ_q . We derive the differentials of χ_l^2 and χ_c^2 first with respect to the parameter set and then with respect to the pixion size. To ensure that the reconstructed image is non-negative, we use logarithm of the pseudo-image $I^{(p)}$.

The derivative of χ_l^2 with respect to $\ln I_i^{(p)}$ is

$$\frac{\partial \chi_l^2}{\partial \ln I_i^{(p)}} = 2I_i^{(p)} \sum_j \frac{R_{l,j}}{\sigma_{l,j}^2} \frac{\partial F_{l,j}}{\partial I_i^{(p)}}, \quad (1)$$

where the residual $R_{l,j}$ is given by

$$R_{l,j} = F_{l,j} - D_{l,j}. \quad (2)$$

The derivative of $F_{l,j}$ with respect to $I_i^{(p)}$ is written as

$$\frac{\partial F_{l,j}}{\partial I_i^{(p)}} = \int \frac{\partial I(\tau)}{\partial I_i^{(p)}} F_c(t_j - \tau) d\tau. \quad (3)$$

We note that

$$\frac{\partial I(\tau)}{\partial I_i^{(p)}} = K_\tau \left(\frac{\tau - \tau_i}{\delta_\tau} \right), \quad (4)$$

which represents the magnitude of the pixion function of pixel τ at pixel i . As a result, we have

$$\frac{\partial F_{l,j}}{\partial I_i^{(p)}} = \int K_\tau \left(\frac{\tau - \tau_i}{\delta_\tau} \right) F_c(t_j - \tau) d\tau. \quad (5)$$

The derivative of the entropy S_l is

$$\frac{\partial S_l}{\partial \ln I_i^{(p)}} = -\alpha \frac{\partial}{\partial \ln I_i^{(p)}} \sum_j \frac{I_j}{I_{\text{tot}}} \ln \frac{I_j}{I_{\text{tot}}} = -\alpha \frac{I_i^{(p)}}{I_{\text{tot}}} \sum_j K_{ji} \left(1 + \ln \frac{I_j}{I_{\text{tot}}} \right), \quad (6)$$

where

$$K_{ji} = \frac{\partial I_j}{\partial I_i^{(p)}} = K_j \left(\frac{\tau_j - \tau_i}{\delta_j} \right). \quad (7)$$

The derivative of χ_l^2 with respect to the continuum pseudo-image $F_{c,i}^{(p)}$ is

$$\begin{aligned} \frac{\partial \chi_l^2}{\partial F_{c,i}^{(p)}} &= 2 \sum_j \frac{R_{l,j}}{\sigma_{l,j}^2} \frac{\partial F_{l,j}}{\partial F_{c,i}^{(p)}} \\ &= 2 \sum_j \frac{R_{l,j}}{\sigma_{l,j}^2} \int I(\tau) \frac{\partial F_c(t_j - \tau)}{\partial F_{c,i}^{(p)}} d\tau \\ &= 2 \sum_j \frac{R_{l,j}}{\sigma_{l,j}^2} \int I(\tau) K_m \left(\frac{t_j - t_i - \tau}{\delta_m} \right) d\tau, \end{aligned} \quad (8)$$

where K_m and δ_m are the pixion function and size appropriate at $t_j - \tau$, respectively. Since we use a uniform pixion size for continuum reconstruction, K_m and δ_m are the same over all pixels. Using the chain rule for differentiation, the derivatives of χ_l^2 with respect to ξ_q and ξ_q are given by

$$\begin{aligned} \frac{\partial \chi_l^2}{\partial \xi_s} &= \frac{\partial \mathbf{F}_c}{\partial \xi_s} \frac{\partial \chi_l^2}{\partial \mathbf{F}_c} \\ &= 2 \mathbf{Q}^{1/2} \sum_j \frac{R_{l,j}}{\sigma_{l,j}^2} \frac{\partial F_{l,j}}{\partial \mathbf{F}_c} \\ &= 2 \mathbf{Q}^{1/2} \sum_j \frac{R_{l,j}}{\sigma_{l,j}^2} \int I(\tau) \frac{\partial F_c(t_j - \tau)}{\partial \mathbf{F}_c} d\tau \\ &= 2 \mathbf{Q}^{1/2} \sum_j \frac{R_{l,j}}{\sigma_{l,j}^2} I(t_j - \mathbf{t}). \end{aligned} \quad (9)$$

and

$$\frac{\partial \chi_l^2}{\partial \xi_q} = \frac{\partial \mathbf{F}_c}{\partial \xi_q} \frac{\partial \chi_l^2}{\partial \mathbf{F}_c} = 2 \left[(\mathbf{L} - \mathbf{S}\mathbf{C}^{-1}\mathbf{L})\mathbf{C}_q^{1/2} \right]^T \sum_j \frac{R_{l,j}}{\sigma_{l,j}^2} I(t_j - \mathbf{t}), \quad (10)$$

where the superscript ‘‘T’’ denotes transposition and \mathbf{t} is a vector of time on which the continuum is reconstructed. χ_c^2 does not depend on $I^{(p)}$ and thus $\partial \chi_c^2 / \partial I_i^{(p)} = 0$. The derivative of χ_c^2 with respect to the continuum pseudo-image $F_{c,i}^{(p)}$ reads

$$\frac{\partial \chi_c^2}{\partial F_{c,i}^{(p)}} = 2 \sum_j \frac{R_{c,j}}{\sigma_{c,j}^2} \frac{\partial F_{c,j}}{\partial F_{c,i}^{(p)}} = 2 \sum_j \frac{R_{l,j}}{\sigma_{l,j}^2} K_j \left(\frac{t_j - t_i}{\delta_j} \right), \quad (11)$$

where the residual $R_{c,j}$ is given by

$$R_{c,j} = F_{c,j} - D_{c,j}. \quad (12)$$

For the derivative of χ_l^2 with respect to the pixion size, we have

$$\frac{\partial \chi_l^2}{\partial \delta_i} = \sum_j \frac{2R_{l,j}}{\sigma_{l,j}^2} \int \frac{\partial I(\tau)}{\partial \delta_i} F_c(t_j - \tau) d\tau = \frac{\partial I(\tau_i)}{\partial \delta_i} \sum_j \frac{2R_{l,j}}{\sigma_{l,j}^2} F_c(t_j - \tau_i), \quad (13)$$

where

$$\frac{\partial I(\tau_i)}{\partial \delta_i} = \int \frac{\partial K_l}{\partial \delta_i} I^{(p)}(y) dy. \quad (14)$$

The derivative of the entropy S_l with respect to the pixion size is

$$\frac{\partial S_l}{\partial \delta_i} = -\alpha \frac{\partial}{\partial \delta_i} \sum_j \frac{I_j}{I_{\text{tot}}} \ln \frac{I_j}{I_{\text{tot}}} = -\frac{\alpha}{I_{\text{tot}}} \sum_j \left(1 + \ln \frac{I_j}{I_{\text{tot}}}\right) \frac{\partial I_j}{\partial \delta_i} = -\frac{\alpha}{I_{\text{tot}}} \left(1 + \ln \frac{I_i}{I_{\text{tot}}}\right) \frac{\partial I_i}{\partial \delta_i}, \quad (15)$$

where we neglect the change of α with the pixion size. The derivative of the entropy S_c with respect to the pixion size can be written similarly.

REFERENCES

- Alston, W. N., Fabian, A. C., Kara, E., et al. 2020, *Nature Astronomy*, 4, 597. doi:10.1038/s41550-019-1002-x
- Bellm, E. C., Kulkarni, S. R., Barlow, T., et al. 2019, *PASP*, 131, 068003. doi:10.1088/1538-3873/ab0c2a
- Bentz, M. C., Denney, K. D., Grier, C. J., et al. 2013, *ApJ*, 767, 149. doi:10.1088/0004-637X/767/2/149
- Bentz, M. C., Horne, K., Barth, A. J., et al. 2010, *ApJL*, 720, L46. doi:10.1088/2041-8205/720/1/L46
- Blandford, R. D. & McKee, C. F. 1982, *ApJ*, 255, 419. doi:10.1086/159843
- Cackett, E. M., Gelbord, J., Li, Y.-R., et al. 2020, *ApJ*, 896, 1. doi:10.3847/1538-4357/ab91b5
- Deeming, T. J. 1975, *Ap&SS*, 36, 137. doi:10.1007/BF00681947
- Dexter, J. & Agol, E. 2011, *ApJL*, 727, L24. doi:10.1088/2041-8205/727/1/L24
- Dixon, D. D., Tümer, T. O., Zych, A. D., et al. 1997, *ApJ*, 484, 891. doi:10.1086/304347
- Du, P., Lu, K.-X., Hu, C., et al. 2016, *ApJ*, 820, 27. doi:10.3847/0004-637X/820/1/27
- Du, P., Hu, C., Lu, K.-X., et al. 2014, *ApJ*, 782, 45. doi:10.1088/0004-637X/782/1/45
- Edelson, R., Gelbord, J., Cackett, E., et al. 2019, *ApJ*, 870, 123. doi:10.3847/1538-4357/aaf3b4
- Eke, V. 2001, *MNRAS*, 324, 108. doi:10.1046/j.1365-8711.2001.04253.x
- Grier, C. J., Peterson, B. M., Horne, K., et al. 2013, *ApJ*, 764, 47. doi:10.1088/0004-637X/764/1/47
- Hall, P. B., Sarrouh, G. T., & Horne, K. 2018, *ApJ*, 854, 93. doi:10.3847/1538-4357/aaa768
- Horne, K. 1994, in *ASP Conf. Ser. 69, Reverberation Mapping of the Broad Line Region in Active Galactic Nuclei*, ed. P. M. Gondhalekar, K. Horne, & B. M. Peterson (San Francisco, CA: ASP), 23
- Horne, K., De Rosa, G., Peterson, B. M., et al. 2021, *ApJ*, 907, 76. doi:10.3847/1538-4357/abce60
- Horne, K., Korista, K. T., & Goad, M. R. 2003, *MNRAS*, 339, 367. doi:10.1046/j.1365-8711.2003.06036.x
- Ivezic, Z., Axelrod, T., Brandt, W. N., et al. 2008, *Serbian Astronomical Journal*, 176, 1. doi:10.2298/SAJ0876001I
- Kaspi, S., Smith, P. S., Netzer, H., et al. 2000, *ApJ*, 533, 631. doi:10.1086/308704
- Kelly, B. C. & Shen, Y. 2013, *ApJ*, 764, 45. doi:10.1088/0004-637X/764/1/45
- Korista, K. T. & Goad, M. R. 2019, *MNRAS*, 489, 5284. doi:10.1093/mnras/stz2330
- Krolik, J. H. & Done, C. 1995, *ApJ*, 440, 166. doi:10.1086/175258
- Li, Y.-R., Ho, L. C., & Wang, J.-M. 2011, *ApJ*, 742, 33. doi:10.1088/0004-637X/742/1/33
- Li, Y.-R., Songsheng, Y.-Y., Qiu, J., et al. 2018, *ApJ*, 869, 137. doi:10.3847/1538-4357/aace6b
- Li, Y.-R. & Wang, J.-M. 2018, *MNRAS*, 476, L55. doi:10.1093/mnrasl/sly028
- Li, Y.-R., Wang, J.-M., & Bai, J.-M. 2016, *ApJ*, 831, 206. doi:10.3847/0004-637X/831/2/206
- Li, Y.-R., Wang, J.-M., & Ho, L. C. 2012, *ApJ*, 749, 187. doi:10.1088/0004-637X/749/2/187
- Marconi, A., Risaliti, G., Gilli, R., et al. 2004, *MNRAS*, 351, 169. doi:10.1111/j.1365-2966.2004.07765.x
- Metcalf, T. R., Hudson, H. S., Kosugi, T., et al. 1996, *ApJ*, 466, 585
- Nash, S. G. 1984, *SIAM Journal on Numerical Analysis*, 21, 770. doi:10.1137/0721052
- Peterson, B. M. 1993, *PASP*, 105, 247. doi:10.1086/133140
- Peterson, B. M. 2014, *SSRv*, 183, 253. doi:10.1007/s11214-013-9987-4
- Peterson, B. M., Ferrarese, L., Gilbert, K. M., et al. 2004, *ApJ*, 613, 682. doi:10.1086/423269
- Pijpers, F. P. & Wanders, I. 1994, *MNRAS*, 271, 183. doi:10.1093/mnras/271.1.183
- Pina, R. K. & Puetter, R. C. 1993, *PASP*, 105, 630. doi:10.1086/133207
- Puetter, R. C. 1996, *Proc. SPIE*, 2827, 12. doi:10.1117/12.255082
- Puetter, R. C. & Yahil, A. 1999, *Astronomical Data Analysis Software and Systems VIII*, 172, 307
- Reynolds, C. S., Young, A. J., Begelman, M. C., et al. 1999, *ApJ*, 514, 164. doi:10.1086/306913
- Rybicki, G. B. & Press, W. H. 1992, *ApJ*, 398, 169. doi:10.1086/171845
- Sergeev, S. G., Doroshenko, V. T., Golubinskiy, Y. V., et al. 2005, *ApJ*, 622, 129. doi:10.1086/427820
- Shankar, F., Weinberg, D. H., & Miralda-Escudé, J. 2013, *MNRAS*, 428, 421. doi:10.1093/mnras/sts026

- Skilling, J. 1989, in Proceedings of the 8th MaxEnt Workshop: Maximum Entropy and Bayesian Methods, ed. by J. Skilling (Dordrecht:Springer), 45
- Starkey, D. A., Horne, K., & Villforth, C. 2016, MNRAS, 456, 1960. doi:10.1093/mnras/stv2744
- Sun, M., Xue, Y., Brandt, W. N., et al. 2020, ApJ, 891, 178. doi:10.3847/1538-4357/ab789e
- Uttley P., McHardy I. M., Papadakis I. E., 2002, MNRAS, 332, 231
- Wang, J.-M., Hu, C., Li, Y.-R., et al. 2009, ApJL, 697, L141. doi:10.1088/0004-637X/697/2/L141
- Xiao, M., Du, P., Horne, K., et al. 2018a, ApJ, 864, 109. doi:10.3847/1538-4357/aad5e1
- Xiao, M., Du, P., Lu, K.-K., et al. 2018b, ApJL, 865, L8. doi:10.3847/2041-8213/aadf8f
- Zu, Y., Kochanek, C. S., & Peterson, B. M. 2011, ApJ, 735, 80. doi:10.1088/0004-637X/735/2/80